

Light Meson Form Factors at near Physical Masses

Benjamin J. Owen,¹ Waseem Kamleh,¹ Derek B. Leinweber,¹ M. Selim Mahbub,^{1,2} and Benjamin J. Menadue^{1,3}

¹*Special Research Centre for the Subatomic Structure of Matter (CSSM),
School of Chemistry and Physics, University of Adelaide, South Australia 5005, Australia**

²*Digital Productivity Flagship,
CSIRO, 15 College Road, Sandy Bay, TAS 7005, Australia*

³*National Computational Infrastructure (NCI),
Australian National University, Australian Capital Territory 0200, Australia*

(Dated: October 26, 2021)

The ability for most hadrons to decay via strong interactions prevents the direct measurement of their electromagnetic properties. However, a detailed understanding of how these resonant states feature in scattering processes can allow one to disentangle such information from photo production processes. In particular, there has been increasing interest in the determination of magnetic dipole moments using such methods. In a recent study [1], Gudiño *et al.* provide the first experimental determination of the magnetic dipole moment of the rho meson. To facilitate a comparison with this experimental determination, we present a calculation of the rho meson and pion electromagnetic form factors calculated in the framework of Lattice QCD. Using the PACS-CS 2+1 flavour full QCD gauge field configurations, we are able to access low Q^2 values at near-physical quark masses. Through the use of variational techniques, we control excited state systematics in the matrix elements of the lowest-lying states and gain access to the matrix elements of the first excited state. Our determination of the rho meson $g_\rho = 2.21(8)$ is in excellent agreement with this experimental determination, but with a significantly smaller uncertainty.

I. INTRODUCTION

Understanding how QCD gives rise to the rich and diverse structure of the hadrons remains an ongoing effort both theoretically and experimentally. Probing the electromagnetic structure remains one of the most effective methods. By measuring the electromagnetic form factors of these states, we map out the distribution of charge and magnetism within and gain valuable insight into the underlying dynamics.

Unlike the nucleon and pion, the vast majority of QCD eigenstates are unstable with respect to the strong interaction. This makes experimental determinations of their properties via conventional means impractical due to their short lifetime. Instead one is forced to disentangle resonant state properties from radiative processes in scattering experiments. Recently, there has been interest in extracting magnetic dipole moments [1–3]. In particular, Gudiño *et al.* [1] have been able to provide a determination of the magnetic dipole moment of the rho meson, the first such experimental result for a vector meson.

It is thus timely to consider what results lattice QCD can provide as a comparison. The overwhelming focus within the lattice community has understandably been on the nucleon, and to a lesser extent the pion, where there exists a large body of experimental data [4]. In comparison, there have been only a handful of lattice studies of rho meson structure [5–7] with the majority of these being performed in the quenched approximation to QCD. The only existing calculation with dynamical

quarks was a preliminary calculation [6] by the QCD-SF collaboration using moderate to heavy pion masses and thus insensitive to the chiral dynamics of full QCD. It is also limited to a large value of nontrivial 4-momentum transfer with $Q_{min}^2 = 0.44 \text{ GeV}^2$. Thus, there is an urgent need for a determination of the rho meson form factors at low Q^2 and near-physical quark masses in full QCD to allow for a direct comparison with experiment.

The progress of the past few years had led to lattice studies near or at physical masses and on lattice volumes significantly larger than the states that occupy them. Working in this new regime has reduced the need for chiral extrapolation, but there are new systematics that must be considered to ensure accurate results. As quark masses decrease, signal weakens and so one is forced to work in early Euclidean-time regions where excited state contamination can be significant. Several studies have explored new approaches to properly handle excited state contaminations with the most popular of these being the summation method [8, 9] and the variational approach [10–16]. Here we make use of the variational approach.

In our recent work [12], we demonstrated how this method provides improved plateau quality and early onset of ground state dominance without the need for the fine-tuning of source and sink operators. Furthermore, this improvement allows us to probe the system at earlier Euclidean times giving rise to significant improvement in the statistical uncertainties. Preliminary studies of electromagnetic properties [15, 16] provide similar conclusions.

In this work we present a calculation of the rho-meson and pion form factors utilising variational methods allowing for an accurate determination of these quantities at near-physical masses. Furthermore the variational

* benjamin.owen@adelaide.edu.au

approach gives us access to the form factors of excited states. The use of moderately large lattice volumes allows us to extract our results at low Q^2 .

For the extraction of the form factors we follow the electromagnetic form factor formalism of Hedditch *et al.* [5] with the necessary changes required for use within the variational approach.

The remainder of this paper is organized as follows. In Section 2 we discuss the use of correlation matrix techniques in the evaluation of hadron matrix elements. In Section 3 we outline the framework used to extract the pion (pseudoscalar) and rho-meson (vector) form factors on the lattice, while Section 4 summarises the details of our lattice simulation. In Section 5 we present our results and finally in Section 6 we provide concluding remarks.

II. THEORETICAL FORMALISM

On the lattice, the determination of hadronic observables begins with the evaluation of the Euclidean-time two and three-point correlation functions. Given an interpolator $\chi(x)$ for the state in question, the two-point function is defined as

$$G(\vec{p}, t) = \sum_{\vec{x}} e^{-i\vec{p}\cdot\vec{x}} \langle \Omega | \chi(x) \chi^\dagger(0) | \Omega \rangle, \quad (1)$$

and the three-point function

$$G_{\mathcal{O}}(\vec{p}', \vec{p}, t_2, t_1) = \sum_{\vec{x}_2, \vec{x}_1} e^{-i\vec{p}'\cdot(\vec{x}_2-\vec{x}_1)} e^{-i\vec{p}\cdot\vec{x}_1} \times \langle \Omega | \chi(x_2) \mathcal{O}(x_1) \chi^\dagger(0) | \Omega \rangle, \quad (2)$$

where \mathcal{O} is the current used to probe the state. Here we are interested in the electromagnetic current $\mathcal{O} = J^\mu$. In general, this interpolator $\chi(x)$ will have overlap with all eigenstates consistent with the given quantum numbers. Inserting a complete set of states between our interpolators in Eq. (1)

$$G(\vec{p}, t) = \sum_{\alpha} e^{-E_{\alpha}(\vec{p})t} \langle \Omega | \chi(0) | \alpha, p \rangle \langle \alpha, p | \chi^\dagger(0) | \Omega \rangle,$$

we can see that the contribution to the correlation function from each state, α , is exponentially suppressed by its energy. The standard approach for examining the ground state is to work at large Euclidean time where excited states are suppressed. In the past this approach has been sufficient for most quantities considered, but with ensembles at near physical masses and studies seeking precision determinations of hadronic observables, there has been increased concern as to whether Euclidean time evolution is a sufficient measure for eliminating excited state effects [17–19]. In this study we select the variational approach to isolate the individual contribution of a particular eigenstate to the two and three-point correlators.

The variational method [20, 21] has become a standard approach for the study of the excited state spectrum of QCD. The goal of this approach is to produce a set of operators ϕ^α that couple directly to individual QCD energy eigenstates

$$\langle \Omega | \phi^\alpha | \beta, p \rangle \propto \delta^{\alpha\beta}. \quad (3)$$

The way in which this is achieved is to take an existing basis of operators $\{\chi_i(x) | i = 1, \dots, n\}$ and construct the optimised operators ϕ^α as linear combinations

$$\phi^\alpha(x) = \sum_i v_i^\alpha \chi_i(x), \quad \phi^{\alpha\dagger}(x) = \sum_j \chi_j^\dagger(x) u_j^\alpha. \quad (4)$$

Beginning with the matrix of two-point correlation functions

$$G_{ij}(\vec{p}, t) = \sum_{\vec{x}} e^{-i\vec{p}\cdot\vec{x}} \langle \Omega | \chi_i(x) \chi_j^\dagger(0) | \Omega \rangle,$$

and making use of Eqs. (3) and (4), both $v_i^\alpha G_{ij}(\vec{p}, t)$ and $G_{ij}(\vec{p}, t) u_j^\alpha$ have a recurrence relation governed by the energy of state α . It follows that the necessary vectors v_i^α and u_j^α are the solutions of the generalised eigenvalue equations

$$v_i^\alpha G_{ij}(\vec{p}, t_0 + \delta t) = e^{-E_\alpha(\vec{p})\delta t} v_i^\alpha G_{ij}(\vec{p}, t_0), \quad (5a)$$

$$G_{ij}(\vec{p}, t_0 + \delta t) u_j^\alpha = e^{-E_\alpha(\vec{p})\delta t} G_{ij}(\vec{p}, t_0) u_j^\alpha. \quad (5b)$$

It is important to note that Eqs. (5a) and (5b) are evaluated for a given 3-momentum \vec{p} and so the corresponding operators satisfy Eq. (3) *for this momentum only*. The correlator for the state $|\alpha, p\rangle$ can be obtained from the correlation matrix by projecting with the relevant eigenvectors

$$G(\vec{p}, t; \alpha) = v_i^\alpha(\vec{p}) G_{ij}(\vec{p}, t) u_j^\alpha(\vec{p}).$$

The extension to three-point correlators follows simply. Beginning with the matrix of three-point correlation functions

$$(G_{\mathcal{O}})_{ij}(\vec{p}', \vec{p}, t_2, t_1) = \sum_{\vec{x}_2, \vec{x}_1} e^{-i\vec{p}'\cdot(\vec{x}_2-\vec{x}_1)} e^{-i\vec{p}\cdot\vec{x}_1} \times \langle \Omega | \chi_i(x_2) \mathcal{O}(x_1) \chi_j^\dagger(0) | \Omega \rangle$$

and having evaluated the eigenvectors with the two-point correlation matrix, it is a simple matter of projecting the necessary eigenvectors onto the matrix of three-point functions, where care is taken to ensure that the projection is done with the correct momenta for source and sink,

$$G_{\mathcal{O}}(\vec{p}', \vec{p}, t_2, t_1; \alpha) \equiv v_i^\alpha(\vec{p}') (G_{\mathcal{O}})_{ij}(\vec{p}', \vec{p}, t_2, t_1) u_j^\alpha(\vec{p}).$$

This applies equally well to hadron transitions ($L \xrightarrow{\mathcal{O}} R$) where one simply projects with relevant eigenvectors for the differing left (L) and right (R) eigenstates.

The application of this approach to states with explicit spin-degrees-of-freedom is straight forward. For a state with spin-1, relevant to this work, the matrix of two-point correlation functions is

$$G_{ij,\sigma\tau}(\vec{p}, t) = \sum_{\vec{x}} e^{-i\vec{p}\cdot\vec{x}} \langle \Omega | \chi_{i,\sigma}(x) \chi_{j,\tau}^\dagger(0) | \Omega \rangle,$$

where the Roman indices denote the operator in the variational basis and the Greek indices denote the Lorentz indices. Following the arguments set out above, we can

construct eigenvalue equations for each Lorentz component and define the corresponding optimised operators as

$$\phi_\sigma^\alpha(x) = \sum_i v_{i,\sigma}^\alpha \chi_{i,\sigma}(x), \quad \phi_\tau^{\alpha\dagger}(x) = \sum_j \chi_{j,\tau}^\dagger(x) u_{j,\tau}^\alpha, \quad (6)$$

i.e. we determine the eigenvectors for each Lorentz component separately such that the operator maximally isolates the spectrum observed in each Lorentz component [22]. Thus our projected two and three-point correlation functions are

$$G_{\sigma\tau}(\vec{p}, t; \alpha) \equiv v_{i,\sigma}^\alpha(\vec{p}) G_{ij,\sigma\tau}(\vec{p}, t) u_{j,\tau}^\alpha(\vec{p}) \\ (G_{\mathcal{O}})_{\sigma\tau}(\vec{p}', \vec{p}, t_2, t_1; \alpha) \equiv v_{i,\sigma}^\alpha(\vec{p}') (G_{\mathcal{O}})_{ij,\sigma\tau}(\vec{p}', \vec{p}, t_2, t_1) u_{j,\tau}^\alpha(\vec{p}).$$

Having obtained the projected two and three-point correlation functions, determination of matrix elements follows in the standard way with the construction of a suitable ratio to isolate the desired terms. We use the ratio defined by Hedditch, *et al.* [5]

$$R_{\sigma^\mu \tau}(\vec{p}', \vec{p}; \alpha) = \sqrt{\frac{\langle G_{\sigma\tau}^\mu(\vec{p}', \vec{p}, t_2, t_1; \alpha) \rangle \langle G_{\tau\sigma}^\mu(\vec{p}, \vec{p}', t_2, t_1; \alpha) \rangle}{\langle G_{\sigma\sigma}(\vec{p}', t_2; \alpha) \rangle \langle G_{\tau\tau}(\vec{p}, t_2; \alpha) \rangle}}, \quad (7)$$

where repeated indices are not summed over. We note that the use of the square root requires the sign of the result to be recovered from the individual three-point functions. Moreover the covariant/contravariant placement of indices is for clarity only. The advantage of this construction is that we have exact cancellation of the momentum-dependent $Z^\alpha(\vec{p})$ factors. In the case of the pseudoscalar pion interpolating field, the $\sigma\tau$ indices are not required and can be ignored.

As in Ref. [5, 23, 24] we consider both $\{U\}$ and $\{U^*\}$ configurations in creating an improved unbiased estimator [25]. This requires the evaluation of both $+\vec{q}$ and $-\vec{q}$ SST-propagators, thus incorporating parity symmetry. A consequence of this is that our correlators are perfectly real or imaginary, depending on the matrix element under consideration. As established in Ref. [25], this approach provides improved plateaus and a reduction of statistical uncertainties beyond a naive doubling of the number of configurations considered.

III. MESON FORM FACTORS

A. Pseudoscalar Mesons

Having defined suitable operators for creating and isolating a particular state α , it now stands to understand how the form factors are extracted from the ratio defined in Eq. (7). We begin this discussion with π meson.

As pseudoscalar mesons are spinless particles, the op-

erator overlap can be decomposed simply

$$\langle \Omega | \phi^{\alpha, \vec{p}}(0) | \pi_\beta(\vec{p}) \rangle = \frac{\delta^{\alpha\beta}}{\sqrt{2E_\alpha(\vec{p})}} Z^\alpha(\vec{p}),$$

where $Z^\alpha(\vec{p})$ enumerates the coupling strength of the operator ϕ^α to the state $|\pi_\beta(\vec{p})\rangle$. It follows that the two-point function can be expressed as

$$G(\vec{p}, t_2; \alpha) = \frac{e^{-E_\alpha(\vec{p}) t_2}}{2E_\alpha(\vec{p})} Z^\alpha(\vec{p}') Z^{\alpha\dagger}(\vec{p}) \quad (8)$$

and the three-point correlation function

$$G^\mu(\vec{p}', \vec{p}, t_2, t_1; \alpha) = \frac{e^{-E_\alpha(\vec{p}') (t_2 - t_1)} e^{-E_\alpha(\vec{p}) t_1}}{2\sqrt{E_\alpha(\vec{p}') E_\alpha(\vec{p})}} \\ \times Z^\alpha(\vec{p}') Z^{\alpha\dagger}(\vec{p}) \langle \pi_\alpha(\vec{p}') | J^\mu(0) | \pi_\alpha(\vec{p}) \rangle, \quad (9)$$

with the matrix element $\langle \pi_\alpha(\vec{p}') | J^\mu(0) | \pi_\alpha(\vec{p}) \rangle$ encoding the interaction vertex of the pion with the electromagnetic current. For a pseudoscalar meson, this vertex is parametrized by a single form factor $G_C(Q^2)$

$$\langle \pi_\alpha(\vec{p}') | J^\mu(0) | \pi_\alpha(\vec{p}) \rangle = \frac{1}{2\sqrt{E_\alpha(\vec{p}') E_\alpha(\vec{p})}} [p'^\mu + p^\mu] G_C^\alpha(Q^2), \quad (10)$$

where p and p' are the incoming and outgoing 4-momenta and $Q^2 = -q^2$ is the space-like momentum transfer. Sub-

stituting Eqs. (8), (9) and (10) into Eq.(7), we obtain

$$R^\mu(\vec{p}', \vec{p}; \alpha) = \frac{1}{2\sqrt{E_\alpha(\vec{p}')E_\alpha(\vec{p})}} [p^\mu + p'^\mu] G_C^\alpha(Q^2).$$

Together with our choice of kinematics, $p' = (E_\alpha, p_x, 0, 0)$ and $p = (m_\alpha, 0, 0, 0)$ with $E_\alpha = \sqrt{m_\alpha^2 + p_x^2}$, we access $G_C^\alpha(Q^2)$ through

$$G_C^\alpha(Q^2) = \frac{2\sqrt{m_\alpha E_\alpha}}{E_\alpha + m_\alpha} R^0(\vec{p}_x, 0; \alpha). \quad (11)$$

which satisfies the spin sum relation

$$\sum_s \epsilon_\sigma^\alpha(p, s) \epsilon_\tau^{\alpha*}(p, s) = - \left(g_{\sigma\tau} - \frac{p_\sigma p_\tau}{m_\alpha^2} \right). \quad (12)$$

B. Vector Mesons

For a vector meson, the overlap term now includes the spin polarization vector $\epsilon(p, s)$

$$\langle \Omega | \phi_\sigma^{\alpha, \vec{p}}(0) | \rho_\beta(\vec{p}, s) \rangle = \frac{\delta^{\alpha\beta}}{\sqrt{2E_\alpha(\vec{p})}} \mathcal{Z}^\alpha(\vec{p}) \epsilon_\sigma^\alpha(p, s),$$

Using these expressions, the two-point function takes the form

$$G_{\sigma\tau}(\vec{p}, t_2; \alpha) = - \frac{e^{-E_\alpha(\vec{p}) t_2}}{2E_\alpha(\vec{p})} \mathcal{Z}^\alpha(\vec{p}) \mathcal{Z}^{\alpha\dagger}(\vec{p}) \left(g_{\sigma\tau} - \frac{p_\sigma p_\tau}{m_\alpha^2} \right), \quad (13)$$

while the three-point correlation function is

$$G_{\sigma\tau}^\mu(\vec{p}', \vec{p}, t_2, t_1; \alpha) = \frac{e^{-E_\alpha(\vec{p}')(t_2-t_1)} e^{-E_\alpha(\vec{p}) t_1}}{2\sqrt{E_\alpha(\vec{p}')E_\alpha(\vec{p})}} \mathcal{Z}^\alpha(\vec{p}) \mathcal{Z}^{\alpha\dagger}(\vec{p}) \epsilon_\sigma^{\prime\alpha}(p', s') \langle \rho_\alpha(\vec{p}', s') | J^\mu(0) | \rho_\alpha(\vec{p}, s) \rangle \epsilon_\tau^{\alpha*}(p, s), \quad (14)$$

where again the matrix element $\langle \rho_\alpha(\vec{p}', s') | J^\mu(0) | \rho_\alpha(\vec{p}, s) \rangle$ contains all of the information governing the interaction with the electromagnetic current. For a spin-1 system, the interaction vertex can be described by three independent vertex functions [26–28]

$$\langle \rho_\alpha(\vec{p}', s') | J^\mu(0) | \rho_\alpha(\vec{p}, s) \rangle = \frac{1}{2\sqrt{E_\alpha(\vec{p})E_\alpha(\vec{p}')}} \epsilon_\delta^{\prime\alpha*}(p', s') \Gamma^{\delta\mu\gamma}(p', p) \epsilon_\gamma^\alpha(p, s) \quad (15)$$

where

$$\Gamma^{\delta\mu\gamma}(p', p) = - \left\{ g^{\delta\gamma} [p^\mu + p'^\mu] G_1(Q^2) + [g^{\gamma\mu} q^\delta - g^{\delta\mu} q^\gamma] G_2(Q^2) - q^\delta q^\gamma \frac{p^\mu + p'^\mu}{2m_\alpha^2} G_3(Q^2) \right\}.$$

Taking the appropriate linear combination of these vertex functions, we arrive at the Sachs decomposition [27, 28]

$$\begin{aligned} G_Q(Q^2) &= G_1(Q^2) - G_2(Q^2) + (1 + \eta) G_3(Q^2), \\ G_M(Q^2) &= G_2(Q^2), \\ G_C(Q^2) &= G_1(Q^2) + \frac{2}{3} \eta G_Q(Q^2), \end{aligned}$$

where $\eta = \frac{Q^2}{4m_\alpha^2}$.

Substituting the vertex into Eq. (14) and applying Eq. (12), the three-point function becomes

$$G_{\sigma\tau}^\mu(\vec{p}', \vec{p}, t_2, t_1; \alpha) = \frac{e^{-E_\alpha(\vec{p}')(t_2-t_1)} e^{-E_\alpha(\vec{p}) t_1}}{2\sqrt{E_\alpha(\vec{p}')E_\alpha(\vec{p})}} \mathcal{Z}^\alpha(\vec{p}) \mathcal{Z}^{\alpha\dagger}(\vec{p}) \mathcal{A}_{\sigma\tau}^\mu(\vec{p}', \vec{p}),$$

where we have grouped all covariant indices into the term

$$\mathcal{A}_{\sigma\tau}^\mu(\vec{p}', \vec{p}) = \left(g_{\sigma\delta} - \frac{p'_\sigma p'_\delta}{m_\alpha^2} \right) \Gamma^{\delta\mu\gamma}(p', p) \left(g_{\gamma\tau} - \frac{p_\gamma p_\tau}{m_\alpha^2} \right).$$

Using the symmetry property $\mathcal{A}_{\sigma}^{\mu}{}_{\tau}(\vec{p}', \vec{p}) = \mathcal{A}_{\tau}^{\mu}{}_{\sigma}(\vec{p}, \vec{p}')$ and our choice of kinematics, the ratio, defined by Eq. (7), becomes

$$R_{\sigma}^{\mu}{}_{\tau}(\vec{p}_x, 0) = \frac{1}{2\sqrt{m_{\alpha}E_{\alpha}}} \left(\frac{p'_{\sigma}p'_{\sigma}}{m_{\alpha}^2} - g_{\sigma\sigma} \right)^{-1/2} \mathcal{A}_{\sigma}^{\mu}{}_{\tau}(\vec{p}_x, 0).$$

In particular we consider

$$\begin{aligned} \mathcal{A}_1^0{}_{1}(\vec{p}_x, 0) &= \frac{E_{\alpha}}{m_{\alpha}} \left((E_{\alpha} + m_{\alpha}) G_C(Q^2) + \frac{2}{3} \frac{p_x^2}{m_{\alpha}} G_Q(Q^2) \right), \\ \mathcal{A}_2^0{}_{2}(\vec{p}_x, 0) = \mathcal{A}_3^0{}_{3}(\vec{p}_x, 0) &= \left((E_{\alpha} + m_{\alpha}) G_C(Q^2) - \frac{1}{3} \frac{p_x^2}{m_{\alpha}} G_Q(Q^2) \right), \\ \mathcal{A}_1^3{}_{3}(\vec{p}_x, 0) &= -\frac{E_{\alpha}}{m_{\alpha}} p_x G_M(Q^2), \\ \mathcal{A}_3^3{}_{1}(\vec{p}_x, 0) &= +p_x G_M(Q^2). \end{aligned}$$

As such, the form factors for the rho meson are isolated from the following combination of ratio terms

$$G_C(Q^2) = \frac{2}{3} \frac{\sqrt{E_{\alpha}m_{\alpha}}}{E_{\alpha} + m_{\alpha}} (R_1^0{}_{1} + R_2^0{}_{2} + R_3^0{}_{3}), \quad (16)$$

$$G_M(Q^2) = \frac{\sqrt{E_{\alpha}m_{\alpha}}}{p_x} (R_3^3{}_{1} - R_1^3{}_{3}), \quad (17)$$

$$G_Q(Q^2) = \frac{m_{\alpha}\sqrt{E_{\alpha}m_{\alpha}}}{p_x^2} (2R_1^0{}_{1} - R_2^0{}_{2} - R_3^0{}_{3}). \quad (18)$$

C. Extracting Static Quantities

The Sachs form factors G_C , G_M and G_Q describe the distribution of charge, magnetism and charge asymmetry within the hadron. In particular, the value of these functions at $Q^2 = 0$ define the hadron's total charge, q , magnetic moment, μ , and quadrupole moment, Q ,

$$q = e G_C(0), \quad (19a)$$

$$\mu = \frac{e}{2m} G_M(0), \quad (19b)$$

$$Q = \frac{e}{m^2} G_Q(0), \quad (19c)$$

where m is the mass of the hadron. In this calculation, we work with fixed-current SST-propagators. This allows us to explore the form factors of many different hadrons without the need for additional inversions, but limits us to a single 3-momentum transfer and thus a single Q^2 for each quark mass.

We make use of a monopole ansatz for the Q^2 dependence

$$G_i(Q^2) = \left(\frac{\Lambda^2}{\Lambda^2 + Q^2} \right) G_i(Q^2 = 0), \quad (20)$$

as suggested by a Vector Dominance Model hypothesis. Here we use a conserved current, $G_C(Q^2 = 0) = 1$, and so we extract the monopole squared-mass Λ^2 via

$$\Lambda^2 = \frac{Q^2}{1 - G_C(Q^2)} G_C(Q^2). \quad (21)$$

Motivated by the observed scaling behaviour for G_E and G_M of the nucleon at low Q^2 , we shall assume the meson sector displays similar scaling for each quark sector and use this to extract a value for $G_M(Q^2 = 0)$

$$G_i(Q^2 = 0) = \frac{G_i(Q^2)}{G_C(Q^2)}, \quad (22)$$

to facilitate a comparison with the experimental prediction of [1] and model expectations. Drawing on the monopole ansatz, we shall also use this for G_Q .

For the mean squared charge radius, we use the standard definition from the small Q^2 expansion of the Fourier transform of the charge distribution which gives

$$\langle r^2 \rangle = -6 \frac{d}{dQ^2} G_C(Q^2) \Big|_{Q^2=0}. \quad (23)$$

Using our monopole form we have

$$\langle r^2 \rangle = \frac{6}{Q^2} \left(\frac{1}{G_C(Q^2)} - 1 \right). \quad (24)$$

IV. SIMULATION DETAILS

Two and three-point correlation functions are evaluated following the prescription outlined in [23, 24, 29, 30]. For this calculation we make use of the PACS-CS (2+1)-flavour dynamical-QCD gauge field configurations [31]

TABLE I. Ensemble parameters used in this calculation.

κ_{ud}	m_π (MeV)	N_{cfgs}	N_{srCs}
0.13700	702	350	350
0.13727	570	350	350
0.13754	411	350	700
0.13700	296	350	700
0.13781	156	197	~ 1600

made available through the ILDG [32]. These configurations are generated using a non-perturbatively $\mathcal{O}(a)$ -improved Wilson fermion action and Iwasaki gauge action on a $32^3 \times 64$ lattice with periodic spatial boundary conditions. The scale is determined via the static quark potential. The value $\beta = 1.90$ gives a lattice spacing $a = 0.0907(13)$ fm resulting in a physical volume of spacial extent $L = 2.9$ fm. We have access to 5 light-quark masses, with the strange quark mass held fixed. The resulting pion masses range from 702 MeV to 156 MeV.

A fixed boundary condition is applied to the temporal direction and our quark sources are inserted at $t_{\text{src}} = 16$. We have verified that reflections associated with the fixed boundary are negligible at Euclidean times greater than 16 time slices away from the boundary. Due to the limited number of configurations at the lightest mass we make use of multiple quark sources on each configuration. This is done by using two maximally separated spacial sources with a relative temporal boundary shift of 8 time slices. The temporal boundary is then shifted by multiples of 16 time slices for each of these spacial sources. Multiple sources are also used for the next two lightest quark masses with a single spacial position, separated temporally by 32 time slices. Table I provides a summary of the simulation details for each κ -value and the corresponding value for m_π^2 .

The three-point correlation functions are evaluated using a sequential source technique with the current held fixed as outlined in [23, 24, 29, 30]. For the current we use an $\mathcal{O}(a)$ -improved conserved vector current obtained using the Noether procedure with the improvement term constructed in the form of a total four-divergence [23, 33]. The current is inserted at $t_c = 21$ relative to the quark insertion time at $t_{\text{src}} = 16$. The resulting source-current separation would in general be too small and so give rise to excited state contamination, but as was highlighted in [12] our use of the variational approach gives rise to rapid ground state dominance after the source allowing for considerably early current insertion and smaller source-current-sink separations.

Given our choice of correlation-function ratio, we require SST-propagators for both $+\vec{q}$ and $-\vec{q}$ where we choose $\vec{q} = \frac{2\pi}{L}\hat{x}$. The current is polarized with $\mu = 3, 4$ as required by our evaluations of the form factors. As outlined in Ref. [25], the invariance of the lattice action under $U \rightarrow U^*$ implies the link variables $\{U\}$ and $\{U^*\}$ are of equal weight and so we choose to account for both

sets of configurations in the evaluation of our correlation functions. Rather than performing further matrix inversions on the $\{U^*\}$ configurations, we make use of the fermion matrix property

$$M(\{U^*\}) = (\tilde{C} M(\{U\}) \tilde{C}^{-1})^*$$

with $\tilde{C} = C\gamma_5$ to give us the propagators for the $\{U^*\}$ from the existing $\{U\}$ propagators [23]

$$S(x, 0; U^*) = (\tilde{C} S(x, 0; U) \tilde{C}^{-1})^*.$$

For the fixed-current SST-propagators this identity takes the form

$$S(x, 0; t, \vec{q}, \mu; U^*) = (\tilde{C} S(x, 0; t, -\vec{q}, \mu; U) \tilde{C}^{-1})^*.$$

Thus, both \vec{q} and $-\vec{q}$ momentum insertions are required as discussed at the end of Section 2. Our error analysis is performed using a second-order jackknife where the χ^2/dof for our fits is obtained through the covariance matrix.

As the primary goal of this work is to cleanly extract matrix elements of the ground state, we choose to work with a small variational basis. Our operators are local meson operators of varying widths. This is achieved by applying increasing levels of gauge invariant Gaussian smearing [34] to our quark sources and sinks. The smearing procedure is:

$$\psi_i(x, t) = \sum_{x'} F(x, x') \psi_{i-1}(x', t), \quad (25)$$

where

$$F(x, x') = (1 - \alpha) \delta_{x, x'} + \frac{\alpha}{6} \sum_{\mu=1}^3 [U_\mu(x) \delta_{x', x+\hat{\mu}} + U_\mu^\dagger(x - \hat{\mu}) \delta_{x', x-\hat{\mu}}], \quad (26)$$

where the parameter $\alpha = 0.7$ is used in our calculation. We use the four different levels of smearing examined in Ref. [35] to provide an optimal basis for these ensembles. Table II lists the corresponding RMS radii for the quark sources. We focus on a single spin-flavour construction for the meson interpolators and draw on the various source/sink smearing widths to enable the efficient and accurate isolation of states in the variational approach. The use of a variety of widths enables the resulting operators to form nodal structures in the radial wave functions of the excited states [36] and is central to our ability to rapidly isolate states in our two- and three-point correlation functions.

For the spin-flavour form of our local interpolator we choose to use,

$$\begin{aligned} \chi_\pi(x) &= \bar{d}(x)\gamma_5 u(x) \\ \chi_\rho(x) &= \bar{d}(x)\gamma_i u(x) \end{aligned}$$

for the π and ρ meson respectively. When coupled with our four smearing widths this allows for the construction of up to a 4×4 correlation matrix. The use of the alternate bi-linear forms $\gamma_0\gamma_5$ and $\gamma_0\gamma_i$ was considered, but these were found to not provide any additional basis span when used with more than two smearing levels. We considered all combinations of variational parameters t_0 and δt in range 17-20 and 1-4 respectively where a superposition of states can be used to constrain the analysis. With regard to state isolation and the stability of the analysis, the optimal choice is $t_0 = 17$ and $\delta t = 3$ for the three heavier masses and $t_0 = 17$ and $\delta t = 2$ for the two remaining lighter masses. The use of an earlier t_0 value relative to baryon studies [35, 37, 38] on the same ensembles is unsurprising given the larger energy gaps displayed between the ground state and first excitation in the meson sector.

In performing our variational analysis we choose to use the symmetrisation procedure outlined in Ref. [39]. Namely we exploit the ensemble average symmetry

$$G_{ij}(\vec{p}, t) = G_{ji}(\vec{p}, t),$$

and consider the improved unbiased estimator

$$\frac{1}{2} [G_{ij}(\vec{p}, t) + G_{ji}(\vec{p}, t)]$$

Enforcing this symmetry allows us to re-express the eigenvalue equations (5a) and (5b) in terms of a real symmetric matrix

$$[G^{-1/2}(\vec{p}, t_0)G(\vec{p}, t_0+\delta t)G^{-1/2}(\vec{p}, t_0)]_{ij} w_j^\alpha = e^{-E_\alpha(\vec{p})\delta t} w_j^\alpha.$$

The resulting eigenvectors from this formulation form an orthogonal basis. These orthogonal eigenvectors, $w_i^\alpha(\vec{p})$, can also be obtained from the eigenvectors $u_i^\alpha(\vec{p})$ using

$$w_i^\alpha(\vec{p}) = G_{ij}^{1/2}(\vec{p}, t_0) u_j^\alpha(\vec{p}).$$

Upon normalising this basis, we are able to sort the eigenvectors consistently across jackknife complement sets, and track eigenstates across momenta using the approximate orthogonality condition

$$\vec{w}(\vec{p}')^\alpha \cdot \vec{w}(\vec{p})^\beta \simeq \delta^{\alpha\beta}.$$

Correlators are normalized to be $\sim \mathcal{O}(1)$ by considering

$$\frac{1}{\sqrt{G_{ii}(\vec{p}, t_{src})}} G_{ij}(\vec{p}, t) \frac{1}{\sqrt{G_{jj}(\vec{p}, t_{src})}}.$$

TABLE II. The RMS radii for the various levels of smearing considered in this work.

Sweeps of smearing	RMS radius (fm)
16	0.216
35	0.319
100	0.539
200	0.778

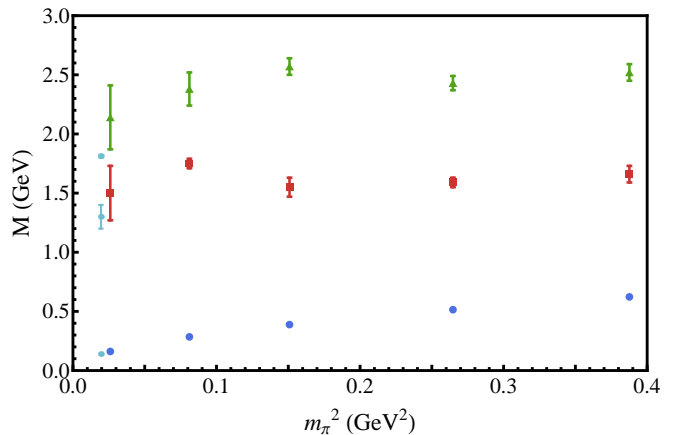


FIG. 1. Low-lying eigenstates in the pion (0^{+-}) channel from our 4×4 correlation matrix of smeared sources and sinks. The left-most points at the physical pion mass are experimental measurements of the spectrum.

The resulting eigenvectors then give us a direct measure of the relative contribution from each interpolator. Accordingly, we also normalise the three-point correlators using the relevant two-point functions

$$\frac{1}{\sqrt{G_{ii}(\vec{p}', t_{src})}} G_{ij}^\mu(\vec{p}', \vec{p}, t_2, t_1) \frac{1}{\sqrt{G_{jj}(\vec{p}, t_{src})}}.$$

V. RESULTS

A. Low lying meson spectrum

In Figs. 1 and 2 we display the resulting spectrum below 3 GeV in the 0^{-+} and 1^{--} channels respectively obtained from the 4×4 correlation matrix of smeared sources and sinks. The masses for the states considered in the form factors analysis are summarised in Table III.

Beginning with the pion channel we find three well separated eigenstates, consistent with the spectrum observed in previous works examining the entire isovector meson sector [40–42]. At the lightest mass we find that our first excited state is consistent with the $\pi(1300)$. A notable feature in our spectrum is a significant shift in the mass for the first excited state at the second lightest mass and a similar jump for the second excited state at the middle mass. This feature is observed across the range of variational parameters considered and on corresponding 3×3 analyses formed from subsets of the variational basis. A similar feature is observed in positive parity spectrum of the nucleon [35, 39]. Examination of the wave functions for these nucleon excitations [36] show significant finite volume effects for the lightest two masses which may give rise to an increase in the eigenstate energies. It is possible that we are observing a similar effect here.

In the rho meson channel, we again observe three well separated eigenstates. However, in this channel we ex-

TABLE III. Masses for the first two π and ρ meson eigenstates (ground state and first excitation) for various values of the hopping parameter, κ , extracted from our 4×4 correlation matrix of smeared sources and sinks.

κ	m_π^2 (GeV ²)	m_π (GeV)	m_ρ (GeV)	m_{π^*} (GeV)	m_{ρ^*} (GeV)
0.13700	0.3876(11)	0.6226(9)	0.981(5)	1.66(7)	1.68(7)
0.13727	0.2647(9)	0.5145(9)	0.917(6)	1.59(4)	1.72(5)
0.13754	0.1509(7)	0.3884(9)	0.867(6)	1.55(8)	1.77(5)
0.13770	0.0811(6)	0.2848(11)	0.832(10)	1.77(4)	1.81(7)
0.13781	0.0260(10)	0.1613(31)	0.793(14)	1.50(23)	1.77(11)

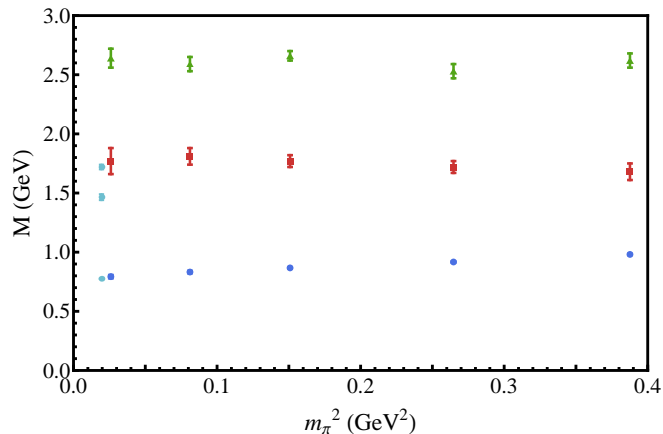


FIG. 2. Low-lying eigenstates in the rho meson (1^-) channel from our 4×4 correlation matrix of smeared sources and sinks. The left-most points at the physical pion mass are experimental measurements of the ρ -meson spectrum.

pect to see two eigenstates near 1600 MeV separated by about 250 MeV. This suggests that a basis of local operators is not able to isolate both of these eigenstates. A similar conclusion was found in Ref. [41]. In Ref. [42] they found that the $\rho(1450)$ required a basis that contained displaced, derivative operators. Quark model expectations predict that for these two states, one is S -wave dominant while the other D -wave dominant [4]. Given the radial symmetry of our operators, it is not possible to form D -wave states and so it is not surprising that we are unable to isolate both states.

The close agreement of our first excited state with the $\rho(1700)$ and the absence of the $\rho(1450)$ from our spectrum suggests that the $\rho(1700)$ is the S -wave state while the $\rho(1450)$ is the D -wave state.

Dudek *et al.* [40] were able to successfully isolate both of these states at larger quark masses and found a trend consistent with our identification of states. They found the S -wave dominated state to be the lighter state at their heavier quark masses, and observed that with decreasing quark mass the mass splitting between these two states became smaller, with the states nearly degenerate at their lightest mass of $m_\pi \simeq 400$ MeV. A continuation of this trend to lighter quark masses places D -wave dominated state lower in mass.

An important feature in the QCD spectrum is the possibility of multi-particle intermediate states. In the infinite-volume limit this renders the majority of hadrons unstable under the strong interaction. However on the finite-volume lattice, the QCD eigenstates are stable and are composed of admixtures of both single-particle and multi-particle states.

Some insight into the composition of states can be taken from the physical spectrum and scattering thresholds. However, the position of these thresholds change on the finite volume. Multi-particle states are forced to overlap in the finite volume, giving rise to a volume-dependent interaction energy. Mixing with single-particle dominated states further distorts the spectrum to the point where intuition from infinite-volume scattering thresholds and the physical spectrum becomes irrelevant, particularly in volumes with lattice length $L \sim 3$ fm.

Below the finite-volume modified two-particle scattering threshold, states are generally single-particle dominated but still contain important contributions from nearby scattering channels. The position of states in the spectrum can be changed by varying the quark mass or the volume of the lattice and the eigenstates can become maximally mixed making their traditional identification as scattering states or resonant states impossible. In the case where a low-lying finite-volume scattering threshold sits well below the resonant state, then the lowest-lying state may be regarded as a two- or multi-particle scattering state and the single-particle dominated state is now the higher eigenstate.

In the case of the vector meson under study here, we must be careful to ensure that the state we are exciting on the lattice is in fact the single-particle dominated resonant state. Though there is strong evidence to suggest that local meson operators couple poorly to scattering states, especially on larger volumes such as that under investigation here, we perform a check to determine whether the eigenstate isolated in our correlation-matrix analysis is single particle in nature.

For all our ensembles, the ground state ρ meson at rest is well below the $\pi\pi$ threshold, and will be single-particle dominated. However, upon applying the boost to momentum \vec{q} , the extracted energy eigenstate now sits above the lowest-lying bare $\pi\pi$ energy allowed by momentum conservation. In order to determine whether the state we have isolated in the boosted case is the finite-volume ρ -

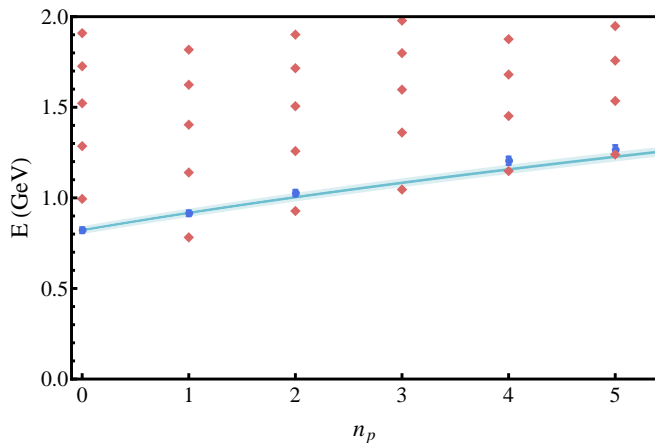


FIG. 3. An example of our comparison between the dispersion relation $E = \sqrt{m^2 + n_p |\vec{p}_{min}|^2}$ (blue line), and the energies extracted from the finite-momentum correlators (blue circles) for the rho meson over a range of momenta. Here m is taken from the zero-momentum correlator, $|\vec{p}_{min}|$ is the magnitude of the lowest non-trivial momentum on the lattice. The red diamonds provide the corresponding non-interacting $\pi\pi$ -energies allowed by momentum conservation. Results at the other values of m_π are similar.

meson or the lower-lying $\pi\pi$ scattering state, we compare the extracted eigenstate energy against the expected energy given by the dispersion relation for a single particle.

In Fig. 3 corresponding to the second-lightest quark mass considered, we overlay the dispersion relation expectation (blue band) with the energies extracted from the finite-momentum correlators (blue data points) for a range of momenta. Here we can see that the energies extracted from the boosted correlator are in excellent agreement with dispersion. This is observed across all the masses considered.

As a further check, we compare the non-interacting $\pi\pi$ energies (red data points) allowed by momentum and parity conservation. For the single unit of lattice momentum relevant to our form factor analysis, we find that the mass separation between the dispersion result and the non-interacting $\pi\pi$ energy is significant. Moreover, the attractive finite-volume interaction in the $\pi\pi$ system would act to further increase the separation between the single and multi-particle dominated states. As a matter of principle, we do expect a $\pi\pi$ scattering state to reveal itself in the long Euclidean-time tail of our correlation function. However, our interpolating fields have rendered this contribution to be negligible at the finite-Euclidean times considered.

This indicates that our correlation functions are indeed dominated by the resonant-like state of interest and not the lower-lying finite volume scattering state. Similar separations are found for all other masses with the exception of the middle mass. Through this process we have determined that the state we have isolated in the boosted system is in fact the state most closely related

to the resonant ρ meson.

B. Form Factor Determination

A key finding from our calculation of g_A using the variational approach [12], was that the optimised operators obtained from the correlation matrix analysis composed of various smeared source/sink operators gave rise to significant improvement in the quality and duration of plateaus from which the matrix elements were extracted. Comparison with a modest historically-typical choice of smearing highlighted that excited state effects are significant and suppress the value of g_A .

We are able to draw similar conclusions here. In Fig. 4 we present a comparison of the correlation function ratios providing the rho-meson charge, magnetic and quadrupole form factors using both the standard single-source approach with a modest level of smearing and our variational approach.

The magnetic form factor, shown in Fig. 4(b), is the most striking example. Here we see a clear difference in the quality of the plateau. For the correlation matrix approach, single-state dominance follows the current at $t_c = 21$ immediately, allowing fits as early as $t_S = 22$.

For the standard approach, the excited states act to suppress the value of G_M at earlier time slices forcing one to wait until at least $t_S = 24$ before an adequate χ_{dof}^2 is obtained. However, the central values show a systematic upward trend following this time slice and consequently there is no indication that a plateau has been obtained.

Similar conclusions can be drawn for the quadrupole form factor in Fig. 4(c). Here we find that both the correlation matrix and the standard approach give consistent values immediately following the current, but diverge as we move out to later time-slices. Again there is a clear systematic drift in the results obtained using the standard approach and it would be difficult to select a fit region where the form factor can be determined with confidence. Given that we seek a region where the extracted form factor is constant over successive time slices, we can clearly see the improvement offered by the correlation matrix approach.

In the case of the charge form factor, Fig. 4(a), the two methods are in closer agreement and display a similar quality in plateau. In either case, some Euclidean time evolution is required before a plateau is observed, but we find that the correlation matrix approach gives a systematically lower value following the current and plateaus a couple of time-slices earlier than the standard approach.

Though the examples presented are selected to highlight the improvement using the variational method, we see significant improvement across all masses and form factors considered. Through this method we consistently find that one is able to obtain single-state dominance earlier and often with significant improvement in the quality of the plateau. Through the use of the variational

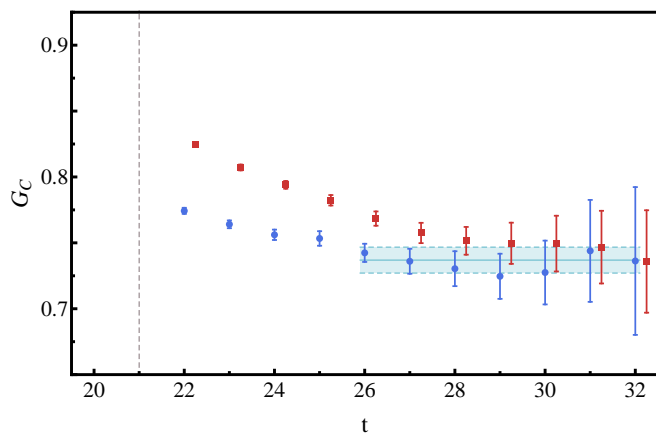
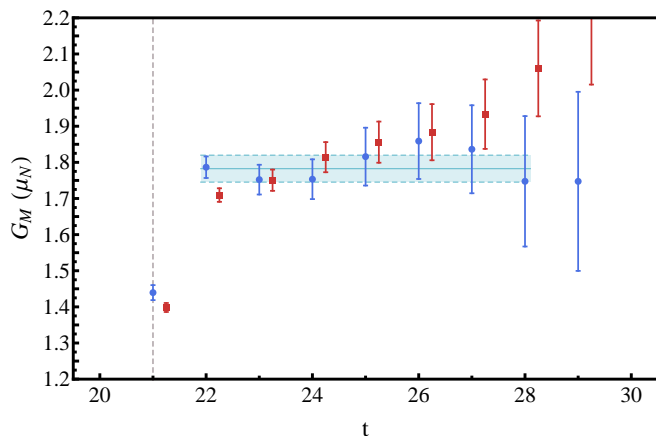
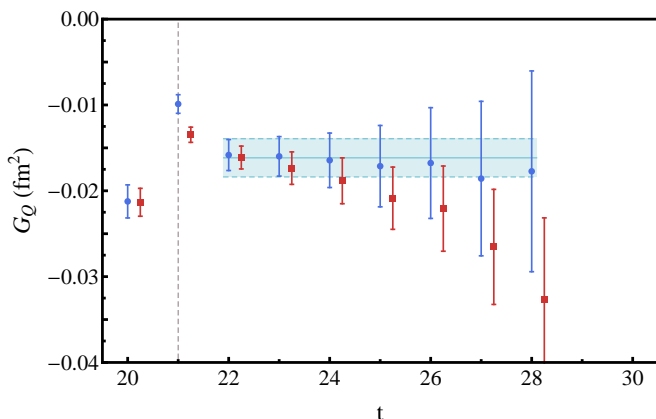
(a) Charge form factor, G_C , for $m_\pi = 296$ MeV.(b) Magnetic form factor, G_M , for $m_\pi = 156$ MeV.(c) Quadrupole form factor, G_Q , for $m_\pi = 296$ MeV.

FIG. 4. A comparison of ρ -meson form factors as a function of Euclidean sink time for a single level of smearing and our variational approach. The data sets obtained from ratios of three- and two-point functions are offset for clarity. The (blue) circles denote the results from the variational approach while the (red) squares illustrate traditional results using the standard single-source method with a moderate level of smearing (35 sweeps). The vertical dashed line indicates the position of the current insertion. The fitted value from the variational approach has been included (shaded band) to highlight where the single source approach is consistent with our improved method.

approach we are able to:

- Isolate an eigenstate at earlier Euclidean times,
- Insert the conserved vector current at earlier Euclidean times,
- Fit the correlation function at earlier Euclidean times,
- Observe robust plateau behaviour,
- Identify large Euclidean-time fit windows,
- Determine the form factors with significantly reduced systematic errors, and
- Determine the form factors with significantly reduced statistical uncertainties due to the admission of analysis at earlier Euclidean times.

C. Form Factors and Static Quantities

In extracting form factors across a wide range of quark masses, it is important to note that for each mass there will be a slight change in the value of Q^2 due to the variation in the mass of the hadron. To ensure that the comparison between quark masses and eigenstates is meaningful, we make use of the monopole ansatz to shift the extracted values for our form factors to a common Q^2 . Fig. 5 demonstrates this shift for the pion. For the pion system, we shift Q^2 values to a common value of $Q^2 = 0.1 \text{ GeV}^2$, while for the ρ -meson system we select $Q^2 = 0.16 \text{ GeV}^2$. These values are selected to minimise the shift for the extractions at the lightest quark mass. We use different values to ensure that we minimise the shift for each system. As the pion is significantly lighter than the ρ meson, a smaller value for Q^2 arises naturally.

Before we examine our form factor results, we note that all quantities presented are the quark sector contributions for unit-charge quarks. Here we choose to label these as the quark sector contributions to the positive-charge eigenstate of the corresponding iso-triplet. That is, the quark contribution is labelled as the u -quark sector while the anti-quark contribution is labelled as the d -quark sector. As we are working with exact isospin symmetry, these quark sector contributions are equivalent and so we choose to present the u -quark sector only. As we are working in full QCD, the hadron form factor will have contributions from the sea quarks. However these contributions have been neglected in our calculation. Thus to make meaningful comparison with experimental data, one should consider the iso-vector quantities,

$$\langle 1_V \rangle = \frac{1}{2}(\langle 1_+ \rangle - \langle 1_- \rangle),$$

where $\langle 1_\pm \rangle$ labels the positive and negative members of the iso-triplet of the pion and ρ meson. However, under exact isospin symmetry one finds that this iso-vector

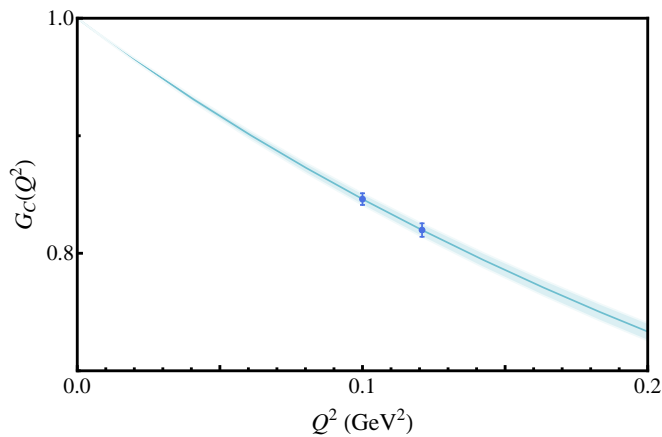


FIG. 5. An example of the shift applied to the pion form factor to ensure that all eigenstates across all quark masses are at a common Q^2 . For the pion and its excitation, this shift is to $Q^2 = 0.10 \text{ GeV}^2$, while for the rho meson and its excitation we shift to $Q^2 = 0.16 \text{ GeV}^2$.

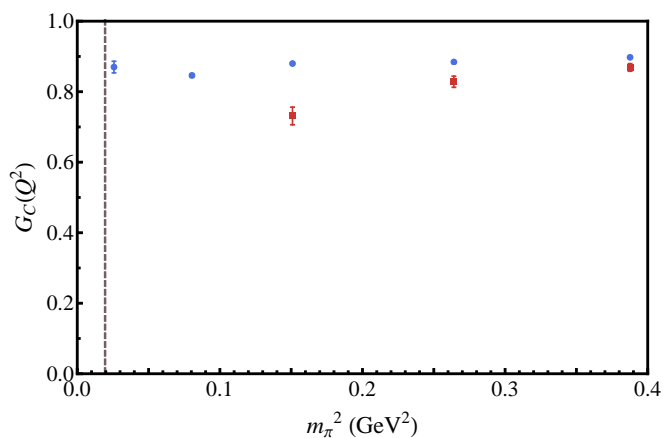


FIG. 6. The unit-charge quark-sector contributions to the charge form factor, G_C , for the pion (blue circles) and its first excitation (red squares) at the common value $Q^2 = 0.10 \text{ GeV}^2$. The dashed line represents the physical point.

quantity defined above is exactly that given by the connected quark sector contribution.

1. Charge Form Factors

In Figs. 6 and 7 we display the charge form factor G_C for the π and π^* mesons and ρ and ρ^* mesons respectively. In both channels we observe a decrease in the charge form factor for the excitation which translates to the excited states having a larger spatial extent. Values are reported in Tables IV and V.

To give us insight into the relative size of these states, we consider the charge radii, shown in Fig. 8. As was found in [5], the ground state vector meson is consistently larger than the corresponding pseudoscalar meson. It was

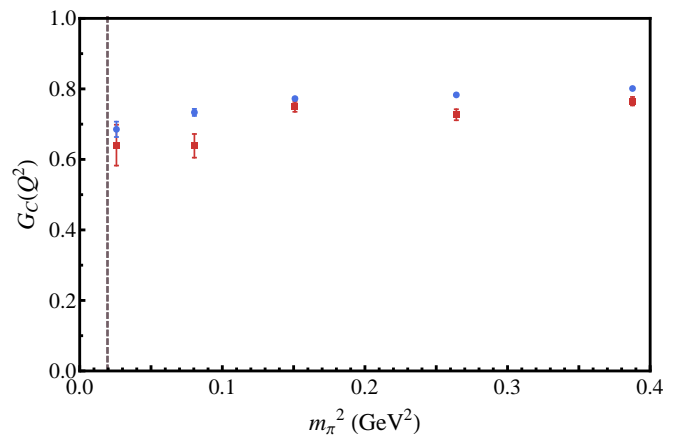


FIG. 7. The unit-charge quark-sector contributions to the charge form factor, G_C , for the rho meson (blue circles) and its first excitation (red squares) at the common value $Q^2 = 0.16 \text{ GeV}^2$.

TABLE IV. The quark sector contributions to the charge form factor, G_C , for the ground state and excited state pi meson, at the common $Q^2 = 0.10 \text{ GeV}^2$. Results are for unit charge quarks.

$m_\pi^2 \text{ (GeV}^2\text{)}$	u_π	u_{π^*}
0.3876(11)	0.898(1)	0.868(11)
0.2647(9)	0.884(2)	0.828(16)
0.1509(7)	0.880(3)	0.731(25)
0.0811(6)	0.846(5)	-
0.0260(10)	0.870(16)	-

noted that this is consistent with quark model expectations where a hyperfine interaction of the form $\frac{\vec{\sigma}_q \cdot \vec{\sigma}_{\bar{q}}}{m_q m_{\bar{q}}}$ is repulsive when spins are aligned and attractive when spins are anti-aligned. In Fig. 10 we also include the experimental value for the pion radius [4], which compares well with our determination.

For the heaviest quark masses where well determined values are available for the excited states, it appears that a similar trend holds between our ρ^* and π^* mesons. The relatively large radii for the excited states at light quark masses are interesting. Results are tabulated in Table VI.

2. Magnetic Form Factors

The magnetic form factors for our ρ and ρ^* mesons are illustrated in Fig. 9. For both the ground and excited state we observe very little variation in the value as m_π varies. As summarised in Table VII, we clearly observe a significantly smaller value of G_M for the excitation. Though we would expect a decrease consistent with the decrease in the charge form factor for this state, the degree of suppression suggests that the magnetic mo-

TABLE V. The quark sector contribution to the charge form factor, G_C , of the ground state and excited state rho meson, at the common $Q^2 = 0.16 \text{ GeV}^2$. Results are for unit charge quarks.

$m_\pi^2 \text{ (GeV}^2\text{)}$	u_ρ	u_{ρ^*}
0.3876(11)	0.801(3)	0.765(12)
0.2647(9)	0.783(3)	0.727(16)
0.1509(7)	0.772(3)	0.749(14)
0.0811(6)	0.733(10)	0.639(34)
0.0260(10)	0.685(22)	0.640(58)

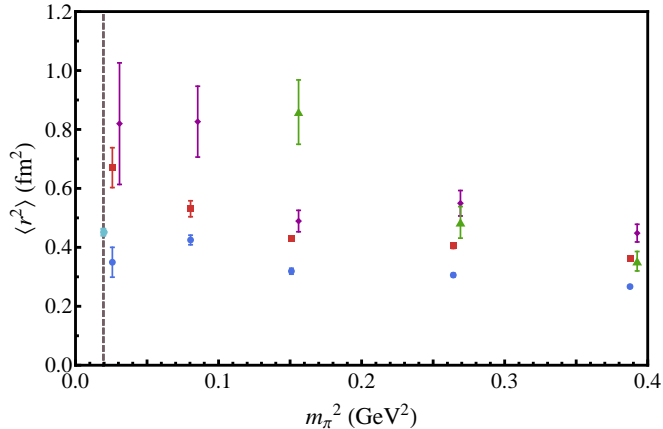


FIG. 8. Mean-square charge radii, $\langle r^2 \rangle$, for the positive-charge states of the π (blue circles), π^* (green triangles), ρ (red squares) and ρ^* (purple diamonds) mesons. The grey dashed line represents the physical point, while the light blue data point is the experimental value for the pion from PDG [4]. The π^* and ρ^* values have been offset for clarity.

ment for this state is smaller than the ground state.

In Table VIII we list magnetic moments for these states where we invoke common scaling between the charge and magnetic form factors. We find a smaller moment for the ρ^* . Our observation is consistent with results for meson magnetic moments using the relativistic Hamiltonian [43] approach. In particular, their value for $\frac{\mu_{2S}}{\mu_{1S}} \simeq 0.7$ compares well with our result of 0.74(9) for the second lightest mass. The quark-mass flow of these magnetic moments is illustrated in Fig. 10.

In Fig. 11 we show the g -factor for the ρ meson, provided by the magnetic moment of the ρ meson in natural magnetons. Constituent quark model expectations suggest for a pure s -wave state, that $g_\rho \simeq 2$. Our result of $g_\rho = 2.21(8)$, taken from our lightest mass point, is larger than this expectation and suggests a non-trivial value for the quadrupole moment of the ρ associated with D -wave mixing. We observe a mild downwards trend of the g -factor with increasing quark mass suggesting that our results are compatible with the quark-model expectation of $g_\rho = 2$ in the large quark mass limit.

Our results agree in value and behaviour with the pre-

TABLE VI. Mean-square charge radii ($\langle r^2 \rangle$) for the positive-charge states of the π and ρ mesons and their first excitations in units of fm^2 .

$m_\pi^2 \text{ (GeV}^2\text{)}$	π	ρ	π^*	ρ^*
0.3876(11)	0.267(4)	0.363(6)	0.35(3)	0.45(3)
0.2647(9)	0.306(7)	0.405(8)	0.48(5)	0.55(4)
0.1509(7)	0.320(10)	0.430(8)	0.86(11)	0.49(4)
0.0811(6)	0.425(16)	0.531(27)	-	0.83(12)
0.0260(10)	0.349(51)	0.670(68)	-	0.82(21)

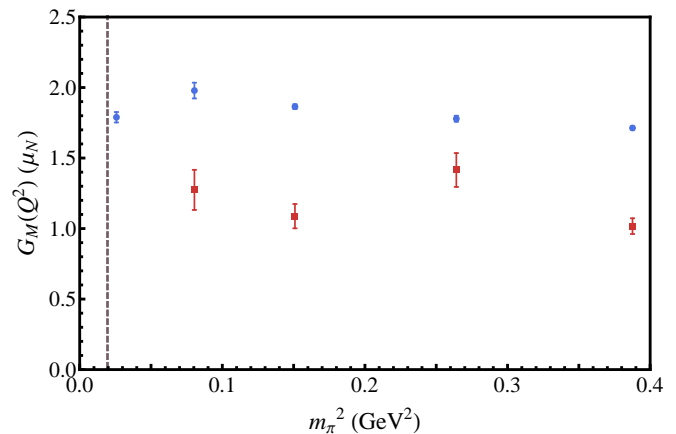


FIG. 9. The unit-charge quark-sector contributions to the magnetic form factor, G_M , of the ρ^+ and ρ^{*+} mesons, at the common $Q^2 = 0.16 \text{ GeV}^2$.

vious quenched determination [5] and dynamical study using background field methods [44]. In Fig. 11 we include the experimental determination of [1]. Within the literature, the majority of model calculations [45–51] give a value of g_ρ between 2.0 and 2.4 similar to our determination of 2.21(8).

3. Quadrupole Form Factors

The quadrupole form factor for the ρ meson is shown in Fig. 12. For the excited ρ^* meson, the signal was too poor to extract a result. As was found in the quenched study of Ref. [5] and the preliminary study of Ref. [6], the quadrupole form factor is negative in value. The value of G_Q varies mildly in the heavy quark regime, however we observe a significant increase in the magnitude as we move to the lightest mass. Numerical results are provided in Table IX.

In Fig. 13 we illustrate the quark mass dependence of the quadrupole moment. We also include the quadrupole moment extracted [52] from the quenched data in Ref. [5]. At heavier masses we find consistent values and find a slight increase in the magnitude in the direction of decreasing quark mass. However, we see a rapid increase in the quadrupole moment magnitude at our lightest mass.

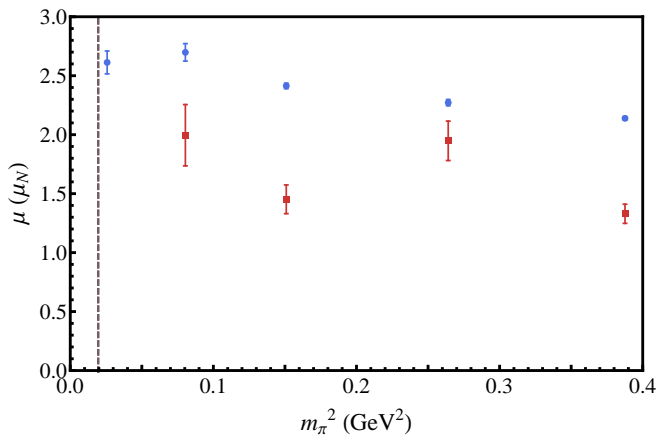


FIG. 10. The quark-mass dependence of the ρ^+ and ρ^{*+} magnetic moments in units of the nuclear magneton.

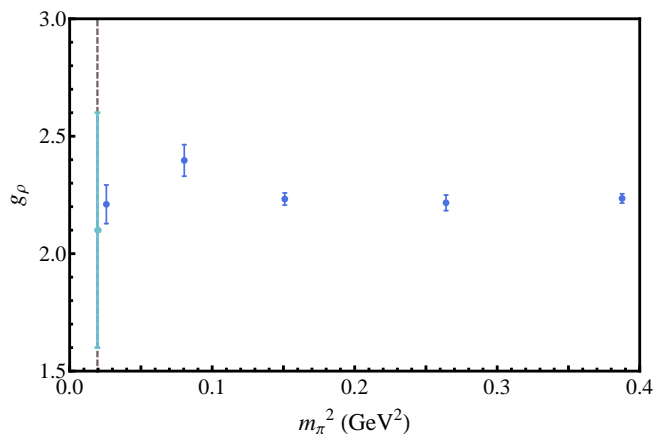


FIG. 11. The g -factor of the ρ meson is provided by the magnetic moment of the ρ meson in natural magnetons. The dashed line highlights the physical point. The light blue data point is the experimental determination of Ref. [1].

The value nearly doubles in comparison with the next lightest mass. This indicates the importance of light-quark dynamics to the underlying structure of the rho meson giving rise to significant contributions from the pion cloud. The dramatic variation observed warrants further investigation into the chiral dynamics of this quantity, especially into the role that finite volume effects may have on the determination.

In Ref. [53], through considerations of the most general free Lagrangian for a charged spin-1 system with minimal electromagnetic coupling, it was shown that there exists an explicit degree of freedom in the Lagrangian which can be parametrised by the g -factor. Consequently one finds that at tree-level the quadrupole moment $Q_\rho = (1 - g_\rho)e/m_\rho^2$. With our value of $g_\rho = 2.21(8)$, the tree-level value for $Q_\rho \simeq -1.21(8)e/m_\rho^2$. In Table X we report the quadrupole moment. To make contact with Ref. [53], we report results in terms of the natural units of e/m_ρ^2 where m_ρ is the mass of the ρ meson observed

TABLE VII. Unit-charge quark-sector contributions to the magnetic form factor of ρ and ρ^* mesons, at the common $Q^2 = 0.16 \text{ GeV}^2$. The natural magneton has been converted to constant units of nuclear magnetons μ_N .

$m_\pi^2 \text{ (GeV}^2\text{)}$	$u_\rho \text{ (}\mu_N\text{)}$	$u_{\rho^*} \text{ (}\mu_N\text{)}$
0.3876(11)	1.713(12)	1.02(6)
0.2647(9)	1.779(21)	1.41(12)
0.1509(7)	1.864(17)	1.09(9)
0.0811(6)	1.978(56)	1.27(14)
0.0260(10)	1.791(37)	-

TABLE VIII. Magnetic moments of the positive-charge states of the ρ and ρ^* mesons in units of nuclear magnetons μ_N .

$m_\pi^2 \text{ (GeV}^2\text{)}$	$\mu_\rho \text{ (}\mu_N\text{)}$	$\mu_{\rho^*} \text{ (}\mu_N\text{)}$
0.3876(11)	2.138(15)	1.33(8)
0.2647(9)	2.272(26)	1.94(17)
0.1509(7)	2.414(23)	1.45(12)
0.0811(6)	2.698(74)	2.00(26)
0.0260(10)	2.613(97)	-

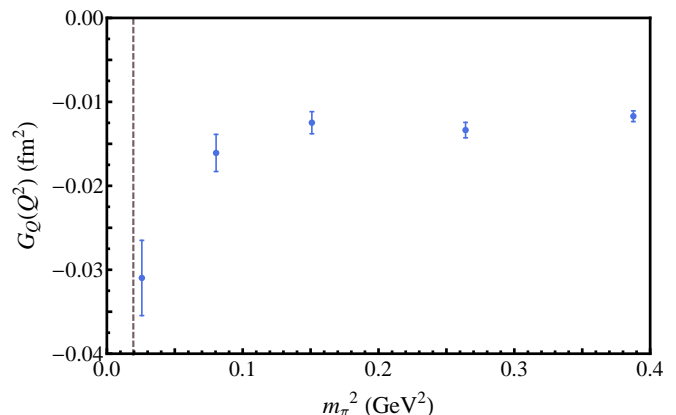


FIG. 12. The unit-charge quark-sector contribution to the quadrupole form factor, G_Q , of the ρ meson at the common $Q^2 = 0.16 \text{ GeV}^2$.

on the lattice at each quark mass. At the lightest quark mass considered we find $Q_\rho = -0.733(99)e/m_\rho^2$ indicating important contributions beyond tree level, driven by the fundamental strong interactions of QCD.

From the perspective of a non-relativistic quark model, the quadrupole moment arises from an admixture of S and D -wave components in the wave function. Thus our non-zero quadrupole moment, even at heavy masses, indicates an important D -wave component to the ρ meson.

In a next-generation calculation where excited-state signals are sufficiently accurate, the quadrupole moment can be used to determine the dominant contributions to the $\rho(1450)$ and $\rho(1700)$ wave functions. Thus, it offers the ideal tag to track these eigenstates with varying quark mass. In this way, one can determine if there is a

TABLE IX. Unit-charge quark-sector contributions to the quadrupole form factor of the ρ meson, at the common $Q^2 = 0.16 \text{ GeV}^2$.

$m_\pi^2 \text{ (GeV}^2\text{)}$	$u_\rho \text{ (fm}^2\text{)}$
0.3876(11)	-0.0117(6)
0.2647(9)	-0.0134(9)
0.1509(7)	-0.0125(13)
0.0811(6)	-0.0161(22)
0.0260(10)	-0.0310(45)

TABLE X. The quadrupole moment of the ρ^+ meson in natural units of e/m_ρ^2 , where m_ρ is the mass of the ρ meson observed on the lattice at each quark mass, and in fixed units of fm^2 .

$m_\pi^2 \text{ (GeV}^2\text{)}$	Q_ρ^{nat}	$Q_\rho \text{ (fm}^2\text{)}$
0.3876(11)	-0.362(20)	-0.0146(8)
0.2647(9)	-0.368(25)	-0.0171(12)
0.1509(7)	-0.313(32)	-0.0162(17)
0.0811(6)	-0.392(53)	-0.0219(30)
0.0260(10)	-0.733(99)	-0.0452(61)

reordering of these states in the light quark regime.

VI. SUMMARY AND CONCLUSIONS

We have established a general framework for the use of the variational approach in the evaluation of hadronic form factors. This approach can be used to systematically eliminate excited state contributions to ground state matrix elements. It also allows one to evaluate the same quantities for excited states with no additional effort.

As we found in Ref. [12], the use of optimised interpolators obtained from the variational approach results in rapid isolation of the eigenstate, enabling earlier insertion of the probing current. Optimised interpolators at the sink result in rapid onset of robust plateau behaviour enabling early and large Euclidean-time fit windows. Together these features act to reduce systematic errors through the suppression of excited state contaminations and reduce statistical uncertainties through the ability to insert the current and establish fit windows earlier in Euclidean time. This approach, coupled with the large lattice volume and light quark masses, has resulted in an accurate determination of the pi and rho electromagnetic form factors at the low Q^2 .

Our light quark-mass determination of the rho-meson g -factor, $g_\rho = 2.21(8)$, compares well with the experimental result of [1], but with significantly smaller uncertainty. This value is consistent with earlier lattice and model evaluations, which collectively prefer a g -factor slightly larger than the simple quark model estimate of 2.

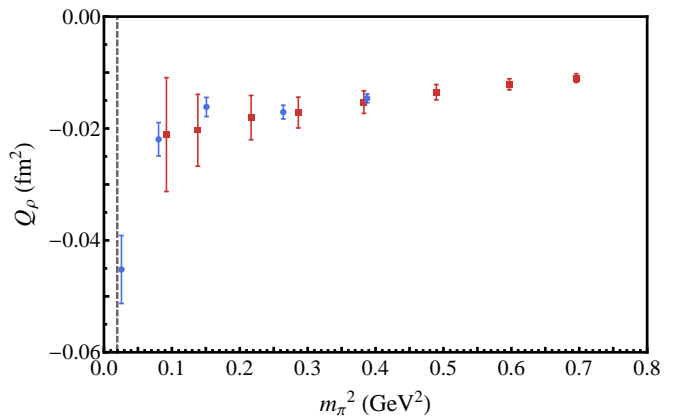


FIG. 13. The quark-mass dependence of the ρ -meson quadrupole moment. The blue circles are from the current analysis, while the red squares are the quenched results from Ref. [5]. We see very similar behaviour between the results at the heavier masses. However, at our lightest mass we observe a significant increase in the magnitude of the quadrupole moment indicating a significant role of the pion cloud in the underlying structure of the rho meson.

As was found in the quenched calculation of Ref. [5], we obtain a negative value for the quadrupole form factor. The onset of significant chiral nonanalytic behaviour in the light quark-mass regime is also observed.

Finally we have for the first time measured the electromagnetic form factors for a light meson excitation. We find that the charge form factors for these states are smaller than their ground state counterparts, consistent with expectations that these states should be larger in size. For the excited rho meson, we observed a significantly smaller value for the magnetic form factor and a smaller magnetic moment for the ρ^* . Our observation of $\mu_{\rho^*}/\mu_\rho = 0.74(9)$ supports the model prediction of Ref. [43].

Future work will investigate the finite-volume corrections to these matrix element calculations drawing on the isolation of spin polarizations in the lattice simulations and effective field theory in relating the finite-volume matrix elements to those realised in Nature.

For the generalised eigenvalue problem with explicit spin degrees of freedom on a finite-volume lattice, one can begin by quantifying the volume-induced non-degeneracies in the spectrum. For boosted eigenstates with spin, there is interplay between the spin polarization direction and the momentum direction. For a fixed momentum direction, the reduced rotational invariance induced by the finite volume of the lattice gives rise to different multi-particle dressings for different polarizations. This gives rise to a subtle variation in the energy of the eigenstates measured using different polarizations. To correctly account for this, a formalism to take the infinite volume limit of each spin-momentum combination considered is to be developed prior to combining the various components to extract the form factors.

Two-point function analyses are in the exploratory phase [54] and the effect is small. Thus, an exploration of the subtle nature of finite-volume corrections await a next-generation simulation. There the role of disconnected quark loop contributions to the form factors can be ascertained.

ACKNOWLEDGEMENTS

We thank PACS-CS Collaboration for making their $2+1$ flavor configurations available and acknowledge the important ongoing support of the ILDG. This research was undertaken with the assistance of resources at the NCI National Facility in Canberra, Australia, and the iVEC facilities at Murdoch University (iVEC@Murdoch) and the University of Western Australia (iVEC@UWA). These resources were provided through the National Computational Merit Allocation Scheme, supported by the Australian Government. We also acknowledge eResearch SA for their support of our supercomputers. This research is supported by the Australian Research Council.

-
- [1] D. G. Gudiño and G. T. Sánchez, (2013), arXiv:1305.6345 [hep-ph].
- [2] G. Lopez Castro and A. Mariano, Phys.Lett. **B517**, 339 (2001), arXiv:nucl-th/0006031 [nucl-th].
- [3] M. Kotulla, J. Ahrens, J. Annand, R. Beck, G. Caselotti, *et al.*, Phys.Rev.Lett. **89**, 272001 (2002), arXiv:nucl-ex/0210040 [nucl-ex].
- [4] J. Beringer *et al.* (Particle Data Group), Phys.Rev. **D86**, 010001 (2012).
- [5] J. Hedditch, W. Kamleh, B. Lasscock, D. Leinweber, A. Williams, *et al.*, Phys.Rev. **D75**, 094504 (2007), arXiv:hep-lat/0703014 [HEP-LAT].
- [6] M. Gurtler *et al.* (QCDSF Collaboration), PoS **LATTICE2008**, 051 (2008).
- [7] C. Alexandrou, P. de Forcrand, and A. Tsapalis, Phys.Rev. **D66**, 094503 (2002), arXiv:hep-lat/0206026 [hep-lat].
- [8] S. Capitani, M. Della Morte, G. von Hippel, B. Jager, A. Juttner, *et al.*, Phys.Rev. **D86**, 074502 (2012), arXiv:1205.0180 [hep-lat].
- [9] S. Capitani, M. Della Morte, G. von Hippel, B. Jager, B. Knippschild, *et al.*, PoS **LATTICE2012**, 177 (2012), arXiv:1211.1282 [hep-lat].
- [10] J. Bulava, M. Donnellan, and R. Sommer, JHEP **1201**, 140 (2012), arXiv:1108.3774 [hep-lat].
- [11] T. Maurer, T. Burch, L. Y. Glozman, C. Lang, D. Mohler, *et al.*, (2012), arXiv:1202.2834 [hep-lat].
- [12] B. J. Owen, J. Dragos, W. Kamleh, D. B. Leinweber, M. S. Mahbub, *et al.*, Phys.Lett. **B723**, 217 (2013), arXiv:1212.4668 [hep-lat].
- [13] B. J. Menadue, W. Kamleh, D. B. Leinweber, M. S. Mahbub, and B. J. Owen, PoS **LATTICE2012**, 178 (2012).
- [14] B. J. Menadue, W. Kamleh, D. B. Leinweber, M. S. Mahbub, and B. J. Owen, (2013), arXiv:1311.5026 [hep-lat].
- [15] B. Owen, W. Kamleh, D. B. Leinweber, S. Mahbub, and B. Menadue, PoS **LATTICE2012**, 173 (2012).
- [16] B. J. Owen, W. Kamleh, D. B. Leinweber, M. S. Mahbub, and B. J. Menadue, PoS **LATTICE2013**, 277 (2013), arXiv:1312.0291 [hep-lat].
- [17] S. Dinter, C. Alexandrou, M. Constantinou, V. Drach, K. Jansen, *et al.*, Phys.Lett. **B704**, 89 (2011), arXiv:1108.1076 [hep-lat].
- [18] H.-W. Lin, PoS **LATTICE2012**, 013 (2012), arXiv:1212.6849 [hep-lat].
- [19] C. Alexandrou, PoS **LATTICE2010**, 001 (2010), arXiv:1011.3660 [hep-lat].
- [20] C. Michael, Nucl.Phys. **B259**, 58 (1985).
- [21] M. Luscher and U. Wolff, Nucl.Phys. **B339**, 222 (1990).
- [22] We note that an analysis accounting for finite-volume systematic errors will need to first construct the spin eigenstates due to finite-volume induced non-degeneracies in the spectrum [54].
- [23] S. Boinepalli, D. Leinweber, A. Williams, J. Zanotti, and J. Zhang, Phys.Rev. **D74**, 093005 (2006), arXiv:hep-lat/0604022 [hep-lat].
- [24] S. Boinepalli, D. Leinweber, P. Moran, A. Williams, J. Zanotti, *et al.*, Phys.Rev. **D80**, 054505 (2009), arXiv:0902.4046 [hep-lat].
- [25] T. Draper, R. Woloshyn, W. Wilcox, and K.-F. Liu, Nucl.Phys.Proc.Suppl. **9**, 175 (1989).
- [26] K. J. Kim and Y.-S. Tsai, Phys.Rev. **D7**, 3710 (1973).
- [27] R. Arnold, C. E. Carlson, and F. Gross, Phys.Rev. **C23**, 363 (1981).
- [28] S. J. Brodsky and J. R. Hiller, Phys.Rev. **D46**, 2141 (1992).
- [29] D. B. Leinweber, R. Woloshyn, and T. Draper, Phys.Rev. **D43**, 1659 (1991).
- [30] D. B. Leinweber, T. Draper, and R. Woloshyn, Phys.Rev. **D46**, 3067 (1992), arXiv:hep-lat/9208025 [hep-lat].
- [31] S. Aoki *et al.*, Phys.Rev. **D79**, 034503 (2009), arXiv:0807.1661 [hep-lat].
- [32] M. G. Beckett *et al.*, Comput.Phys.Commun. **182**, 1208 (2011), arXiv:0910.1692 [hep-lat].
- [33] G. Martinelli, C. T. Sachrajda, and A. Vladikas, Nucl.Phys. **B358**, 212 (1991).
- [34] S. Gusken, Nucl. Phys. Proc. Suppl. **17**, 361 (1990).
- [35] M. S. Mahbub, W. Kamleh, D. B. Leinweber, P. J. Moran, and A. G. Williams (CSSM Lattice collaboration), Phys.Lett. **B707**, 389 (2012), arXiv:1011.5724 [hep-lat].
- [36] D. S. Roberts, W. Kamleh, and D. B. Leinweber, Phys.Rev. **D89**, 074501 (2014), arXiv:1311.6626 [hep-lat].

- [37] B. J. Menadue, W. Kamleh, D. B. Leinweber, and M. S. Mahbub, *Phys.Rev.Lett.* **108**, 112001 (2012), arXiv:1109.6716 [hep-lat].
- [38] M. S. Mahbub, W. Kamleh, D. B. Leinweber, P. J. Moran, and A. G. Williams (CSSM Lattice Collaboration), *Phys.Rev.* **D87**, 011501 (2013), arXiv:1209.0240 [hep-lat].
- [39] M. S. Mahbub, W. Kamleh, D. B. Leinweber, P. J. Moran, and A. G. Williams, *Phys.Rev.* **D87**, 094506 (2013), arXiv:1302.2987 [hep-lat].
- [40] J. J. Dudek, R. G. Edwards, M. J. Peardon, D. G. Richards, and C. E. Thomas, *Phys.Rev.* **D82**, 034508 (2010), arXiv:1004.4930 [hep-ph].
- [41] C. Gattringer, L. Y. Glozman, C. Lang, D. Mohler, and S. Prelovsek, *Phys.Rev.* **D78**, 034501 (2008), arXiv:0802.2020 [hep-lat].
- [42] G. P. Engel, C. Lang, M. Limmer, D. Mohler, and A. Schafer (BGR [Bern-Graz-Regensburg] Collaboration), *Phys.Rev.* **D82**, 034505 (2010), arXiv:1005.1748 [hep-lat].
- [43] A. Badalian and Y. Simonov, *Phys.Rev.* **D87**, 074012 (2013), arXiv:1211.4349 [hep-ph].
- [44] F. X. Lee, S. Moerschbacher, and W. Wilcox, *Phys.Rev.* **D78**, 094502 (2008), arXiv:0807.4150 [hep-lat].
- [45] J. de Melo and T. Frederico, *Phys.Rev.* **C55**, 2043 (1997), arXiv:nucl-th/9706032 [nucl-th].
- [46] M. Bhagwat and P. Maris, *Phys.Rev.* **C77**, 025203 (2008), arXiv:nucl-th/0612069 [nucl-th].
- [47] T. Aliev, A. Ozpineci, and M. Savci, *Phys.Lett.* **B678**, 470 (2009), arXiv:0902.4627 [hep-ph].
- [48] H. Roberts, A. Bashir, L. Gutierrez-Guerrero, C. Roberts, and D. Wilson, *Phys.Rev.* **C83**, 065206 (2011), arXiv:1102.4376 [nucl-th].
- [49] M. Pitschmann, C.-Y. Seng, M. J. Ramsey-Musolf, C. D. Roberts, S. M. Schmidt, *et al.*, *Phys.Rev.* **C87**, 015205 (2013), arXiv:1209.4352 [nucl-th].
- [50] D. Djukanovic, E. Epelbaum, J. Gegelia, and U.-G. Meissner, *Phys.Lett.* **B730**, 115 (2014), arXiv:1309.3991 [hep-ph].
- [51] C. S. Mello, A. Nunes da Silva, J. de Melo, and T. Frederico, *Nucl.Phys.Proc.Suppl.* **251-252**, 62 (2014).
- [52] We note that an error was made in Ref. [5] in converting the lattice form factors from natural units to fixed units.
- [53] T. D. Lee, *Phys. Rev.* **140**, B967 (1965).
- [54] W. Kamleh, D. B. Leinweber, B. J. Owen, J. Wu, and R. D. Young, In preparation.